Complex dynamics of a unidirectional optical oscillator based on a liquid-crystal gain medium

A. Montina,[1] U. Bortolozzo,[2] S. Residori,[3] J. P. Huignard,[4] and F. T. Arecchi[1]

[1]*Dipartimento di Fisica, Università di Firenze, Via Sansone 1, 50019 Sesto Fiorentino, Firenze Italy*
[2]*Laboratoire de Physique Statistique de l'ENS, 24 rue Lhomond, 75231 Paris Cedex 5, France*
[3]*INLN, CNRS, Université de Nice Sophia-Antipolis, 1361 route des Lucioles, 06560 Valbonne, France*
[4]*Thales Research and Technology, RD 128 91767 Palaiseau Cedex, France*

A unidirectional optical oscillator consists of an optical amplifier whose outgoing field is reinjected into the incoming one by means of a ring cavity. We used recently a liquid crystal light valve as optical amplifier and reported experimental evidence of cavity field oscillations. The light-valve provides a high gain and a wide transverse size, activating a large number of cavity modes, both transverse and longitudinal. A mean-field approximation along the cavity axis is not suitable for this system, thus we introduce a model which accounts for the activation of different transverse and longitudinal modes and shows numerically that their interaction generates three-dimensional spatiotemporal pulses localized along the cavity axis. The generation of these pulses is experimentally verified.

PACS number(s): 42.65.Sf, 05.45.−a, 42.70.Df, 61.30.−v

I. INTRODUCTION

A laser is a positive feedback optical amplifier. The active medium with population inversion acts as the light amplifier by means of stimulated emission and the cavity supplies the feedback [1]. The two-wave mixing (2WM) in nonlinear photorefractive crystals provides another mechanism of light amplification [2] and has been intensively used to observe a rich variety of spatiotemporal dynamics of the transverse cavity modes [3]. Because of the limited transverse size of photorefractive crystals, the number of activated modes is relatively small, typically about few tens. Recently, we provided experimental evidence of optical oscillations with a huge number of modes using a liquid crystal light valve (LCLV) as the two-wave mixing device [4].

In this paper we present the full derivation of the model for the unidirectional optical oscillator based on the LCLV as the gain medium. Experimental results, such as the three-dimensional (3D) spatiotemporal pulses, are presented and compared to the theoretical predictions. The model is derived starting from the Maxwell equations for the light propagation in the cavity and from the theory of the LCLV. The main differences with respect to existing models of cavity oscillators [5–7] are due to the specific features of the gain medium. Indeed, due to the large gain and transverse size of the LCLV, a huge number of transverse and longitudinal modes can be simultaneously activated, preventing the use of a mean-field approximation along the cavity axis. Thus, our model considers the effects of different longitudinal modes and accounts for longitudinal variations of the cavity field. We show that the field displays spatiotemporal pulses localized in the transverse and longitudinal directions. Another important difference with previous models for photorefractive ring cavities is the second-order nonlinear coefficient of the refractive index; in photorefractive media it is generally imaginary, but for the LCLV it is always real. This has important consequences on the saturation mechanisms and the dynamical interplay among different modes.

In Sec. II, we give a brief description of the experimental setup. In Sec. III, we introduce the equations for the LCLV and the cavity field. In Sec. IV we analyze the model in the one-mode approximation and recover the mean-field approximation in the limit of a suitably small number of modes. In Sec. V, simulations are presented for a one transverse dimension and a large number of modes, showing the presence of a longitudinal pattern of the cavity field. In Sec. VI, we report the experimental data and provide evidence of longitudinal multimode effects. Finally, in Sec. VII we give the conclusions. Five movies of both numerical and experimental dynamics are available online [8]. Their description will be given in Secs. V and VI.

II. DESCRIPTION OF THE EXPERIMENTAL SETUP

The experimental setup is schematically represented in Fig. 1. The LCLV is composed of a nematic liquid crystal cell with one of the walls made of a slice, 1 mm thick, of the photorefractive $B_{12}SiO_{20}$ (BSO) crystal [9]. An external ac voltage of amplitude V_0 is applied to the liquid crystal cell by means of transparent electrodes deposited over the glass window and the external side of the BSO crystal. The BSO acts as a transparent photoconductor, thus modulating the voltage across the liquid crystals as a function of the intensity of the light passing through the cell [10]. The overall effect is a change of the refractive index n as a function of the imping-ing light intensity I (Kerr nonlinearity). In the first approxi-mation $n = n_c + \alpha I$, where n_c is the constant component and α is the nonlinear coefficient accounting for the Kerr-type ef-
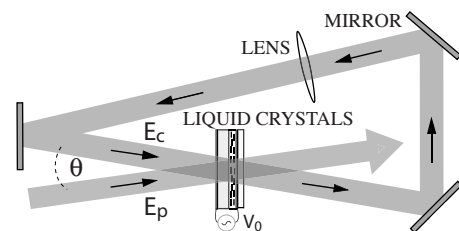

FIG. 1. Experimental setup.

fect. The advantages of the LCLV with respect to other nonlinear media are the high value of α and the large transverse size (in our valve the cell area is 20×30 mm²), allowing the simultaneous amplification of a large number of cavity modes, both transverse and longitudinal.

The LCLV is positioned inside a ring cavity consisting of three high-reflectivity dielectric mirrors. A lens with focal length f is inserted in the cavity in order to fulfill the stability condition $4f > L_{cav}$ and have a discrete spectrum for the transverse modes. The total length of the cavity is $L_{cav} = 240$ cm and the lens has a $f = 70$ cm focal length. The LCLV is pumped by a plane-wave optical beam provided by a diode pumped solid state laser ($\lambda = 532$ nm) and propagating at an angle $\theta \simeq 30$ mrad with respect to the cavity axis.

The light amplification in the cavity is based on two-wave mixing interactions in the liquid crystals [9]. The pump polarization is linear and parallel to the liquid crystal director orientation, which is vertical. The pump induces in the liquid crystal a homogeneous variation of the refractive index $n(\vec{r}_\perp)$, $\vec{r}_\perp$ being the transverse coordinates of the two-dimensional layer. Because of inhomogeneous thermal fluctuations of $n(\vec{r}_\perp)$, a small fraction of light is scattered in the direction of the cavity axis and, after a turn in the ring, it adds to the pump field creating a small grating in $n(\vec{r}_\perp)$. If the losses in the cavity are sufficiently small, this grating scatters a larger fraction of the pump field into the ring and an exponential growth of the cavity field occurs, until saturation effects become relevant. The spontaneously generated cavity field is polarized along the vertical direction, since only the extraordinary waves are amplified by the 2WM [9].

The Fresnel number of the cavity, which is the ratio of the diffraction limiting aperture to the area of the fundamental Gaussian mode, is controlled by a diaphragm placed behind the lens and can be changed from $F = 1$ to approximately $F = 500$, which implies changing from a single transverse mode oscillation to a regime where a huge number of modes are interacting. The number of oscillating modes can be changed also by varying the voltage V_0 applied to the LCLV. Indeed, V_0 changes the uniform refractive index of the LCLV, thus it acts directly on the frequency detuning between the cavity field and the pump beam, which, as we will see in the following, is the main mechanism of mode selection.

For the purpose of visualization, a small fraction (4%) of the cavity field is extracted by a beam sampler and, after passing through a lens, is separated into three distinct optical paths. Three charge-coupled device CCD cameras record the transverse intensity distributions at three different planes, chosen in such a way to image the cavity field at three different planes situated at different z coordinates along the cavity axis.

III. THEORY OF THE MANY-MODE LIQUID CRYSTAL OSCILLATOR

In Sec. III A we study the two-wave mixing interaction in the LCLV and show that it provides an amplification mechanism when one of the fields is much larger than the other one. In Sec. III B, we complete the model of the liquid crys-

tal optical oscillator (LCO) introducing the equations for the ring cavity feedback.

The model is derived by coupling the Maxwell equations with a Debye relaxation equation for the refractive index in the liquid crystal layer. We anticipate that we will end up with two medium equations, one for the slowly varying component of the refractive index, describing the self-interaction of the cavity field, and one for the spatial grating, giving the 2WM mechanism of photon injection inside the cavity. The dynamics of the refractive index depends on the field intensity impinging on the photoconductor side of the LCLV, thus the two medium equations are coupled to an evolution equation for the cavity field, which accounts also for the longitudinal variations along the propagation direction. Because of the large scale separation between the liquid crystal response time and the light round-trip time in the cavity, the field evolution is slaved to that of the refractive index. In Appendix A we describe a numerical method that efficiently solves the cavity field equation.

A. The LCLV as a light amplifier

Let $\vec{r}_\perp$, z be the transverse and normal coordinates of the liquid crystal layer, respectively. The origin of z is positioned at the entrance side of the liquid crystal layer. In a wide range of parameters, the LCLV is characterized by a nearly constant coefficient α. Thus, for a constant impinging light intensity $I(\vec{r}_\perp)$, the uniform refractive index is $n(\vec{r}_\perp) = n_c + \alpha I(\vec{r}_\perp)$. Because of the finite relaxation time τ and the charge carrier diffusion in the photoconductor layer, for time-dependent I the refractive index obeys the following relaxation equation:

$$\tau \dot{n}(\vec{r}_\perp, t) = (-1 + l_0^2 \nabla_\perp^2) n(\vec{r}_\perp, t) + \alpha I(\vec{r}_\perp, t) + n_c, \quad (1)$$

where l_0 is the diffusion length of the charge carriers [11].

Let the impinging light be the superposition of a strong pump beam and a weak one with wave numbers $\vec{k}_p$ and $\vec{k}_c$, respectively. The angle θ between them is small and they are nearly orthogonal to the LCLV. We take a plane pump wave and write the overall electric field as follows:

$$E(\vec{r}, t) = E_p e^{i(\vec{k}_p \cdot \vec{r} - \omega_p t)} + E_c(\vec{r}, t) e^{i(\vec{k}_c \cdot \vec{r} - \omega_p t)} \quad (z < 0), \quad (2)$$

where E_p is a constant amplitude and E_c is slowly varying in time and space with respect to the carrier $e^{i(\vec{k}_c \vec{r} - \omega_p t)}$, with $\omega_p \equiv c|\vec{k}_p| \simeq c|\vec{k}_c|$.

The light intensity arriving at the photoconductive side of the LCLV is

$$|E(\vec{r}, t)|^2 = |E_p|^2 + |E_c(\vec{r}, t)|^2 + [E_p^* E_c(\vec{r}, t) e^{-i\vec{K}_\perp \cdot \vec{r}} + \text{c.c.}], \quad (3)$$

where $\vec{K}_\perp \equiv \vec{k}_p - \vec{k}_c$, which is nearly parallel to the liquid crystal layer. The first two terms generate a slowly varying refractive index, whereas the last one produces a grating with wave number $\vec{K}_\perp$. If the spatial spectral width of E_c is sufficiently smaller than $|\vec{K}_\perp|$, the refractive index can be decomposed as
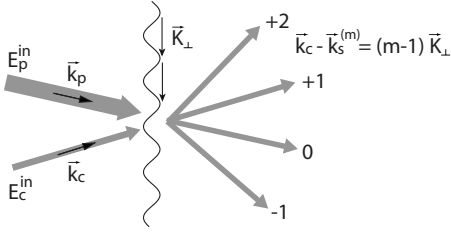
FIG. 2. Multiple scatterings from the refractive index grating; $k_s^{(m)}$ is the wave vector of the m order scattered beam.

$$n(\vec{r}_\perp, t) = \tilde{n} + n_0(\vec{r}_\perp, t) + [n_1(\vec{r}_\perp, t)e^{-i\vec{K}_\perp \cdot \vec{r}_\perp} + \text{c.c.}], \quad (4)$$

where $\tilde{n} \equiv n_c + \alpha I_p$ is a constant term, $I_p \equiv |E_p^{(in)}|^2$ being the pump intensity at the entrance of the LCLV ($z=0$). Replacing this equation into Eq. (1), we obtain the equations for the envelope fields n_0 and n_1,

$$\tau \dot{n}_0 = (-1 + l_0^2 \nabla_\perp^2)n_0 + \alpha |E_c^{(in)}(\vec{r}_\perp, t)|^2, \quad (5)$$

$$\tau \dot{n}_1 = (-c_1 - 2il_0^2 \vec{K}_\perp \cdot \vec{\nabla}_\perp + l_0^2 \nabla_\perp^2)n_1 + \alpha E_p^{(in)*} E_c^{(in)}(\vec{r}_\perp, t), \quad (6)$$

where $E_c^{(in)}(\vec{r}_\perp, t)$ is the cavity field at $z=0$ (entrance side of the LCLV) and $c_1 \equiv 1 + l_0^2 |\vec{K}_\perp|^2$.

Now, we must evaluate the outgoing fields. If the higher scattering orders are negligible, the main effect of the modulation of the refractive index consists in coupling E_p and E_c. A photon in the pump beam can scatter into the cavity field and vice versa. However, if $|\vec{k}_p|d|n_1|$ is not much smaller than 2π, multiple scatterings into higher orders occur and a photon can acquire a transverse wave number which is a multiple of $\vec{K}_\perp$, as schematically depicted in Fig. 2. Because of the high gain of the LCLV, we must account for these higher order scatterings and write the field in the liquid crystal as follows:

$$E(\vec{r}, t) = e^{i(\tilde{n}\vec{k}_p \cdot \vec{r} - \omega_p t)} \sum_{m=-\infty}^{\infty} E_m(\vec{r}, t)e^{-im\vec{K}_\perp \cdot \vec{r}} \quad (z > 0), \quad (7)$$

where m is the order of the scattered wave. At $z=0$, $E_0 = E_p^{(in)}$, $E_1 = E_c^{(in)}$ and the other components are zero. Note that we have multiplied the wave number $\vec{k}_p$ by the uniform refractive index $\tilde{n}$.

In order to fulfill the continuity condition of E and its derivative at the boundary between regions with different refractive index, we should account for reflections. However their effect can be included in the overall losses, which we neglect for the moment. The electric field E in the liquid crystal satisfies the equation

$$\nabla^2 E(\vec{r}, t) - \frac{n^2(\vec{r})}{c^2} \frac{\partial^2 E(\vec{r}, t)}{\partial t^2} = 0. \quad (8)$$

We assume that the component E_c is nearly constant with respect to the optical frequency and neglect the time dependence of the components E_m (adiabatic approximation). Furthermore, the small thickness of the liquid crystal layer and

smallness of n_0 and n_1 enable us to neglect the diffractive terms $\nabla^2 E_m$ and the squares n_0^2 and n_1^2. Since only the first scattering orders are relevant, we can assume the vectors $\vec{k}_p - m\vec{K}_\perp$ nearly parallel to $\vec{k}_p$ in the terms with the gradient of E_c. With these approximations, Eq. (8) becomes

$$\frac{\partial E_m(\vec{r}_\perp, z)}{\partial z} = ik \sum_{l=-1}^{1} n_l E_{m-l}(\vec{r}_\perp, z), \quad (9)$$

where $k \equiv |\vec{k}_p| \simeq |\vec{k}_c|$. The eigenmodes are $E_m^{(s)}(\vec{r}_\perp) = F^{(s)}(\vec{r}_\perp)e^{ism}$, where $s \in [0, 2\pi]$ and F is a complex function. The corresponding eigenvalues are

$$\eta^{(s)}(\vec{r}_\perp) \equiv ik \sum_{l=-1}^{1} n_l(\vec{r}_\perp)e^{-ils}. \quad (10)$$

The general solution of Eq. (9) is

$$E_m(\vec{r}_\perp, z) = \int_0^{2\pi} ds F^{(s)}(\vec{r}_\perp) e^{\eta^{(s)}(\vec{r}_\perp)z} e^{ism}. \quad (11)$$

For $z=0$, $E_0 = E_p^{(in)}$, $E_1 = E_c^{(in)}$ and the remaining components are zero, thus we have that

$$F^{(s)}(\vec{r}_\perp) = \frac{1}{2\pi}(E_p^{(in)} + E_c^{(in)}e^{-is}). \quad (12)$$

By performing the integration in Eq. (11), we find the outgoing fields of E_p and E_c,

$$E_p^{(out)} = e^{i\bar{n}_0}\left[J_0(2|\bar{n}_1|)E_p^{(in)} - i\frac{\bar{n}_1^*}{|\bar{n}_1|}J_{-1}(2|\bar{n}_1|)E_c^{(in)}\right], \quad (13)$$

$$E_c^{(out)} = e^{i\bar{n}_0}\left[J_0(2|\bar{n}_1|)E_c^{(in)} + i\frac{\bar{n}_1}{|\bar{n}_1|}J_1(2|\bar{n}_1|)E_p^{(in)}\right], \quad (14)$$

where J_l are the Bessel functions of order l and where we have introduced the rescaling of the refractive indices

$$kdn_l \rightarrow \bar{n}_l. \quad (15)$$

In general, when there are many input fields $E_l^{(in)}$, the outgoing fields are

$$E_l^{(out)} = e^{i\bar{n}_0}\sum_m \left(i\frac{\bar{n}_1}{|\bar{n}_1|}\right)^m J_m(2|\bar{n}_1|)E_{l-m}^{(in)}. \quad (16)$$

The limit $|\bar{n}_1| \ll 1$ corresponds to the first diffraction order, where photons undergo at most only one scattering process. In this limit, Eqs. (13) and (14) become (with $|E_p^{(in)}| \gg |E_c^{(in)}|$)

$$E_p^{(out)} \simeq e^{ikn_0 d}E_p^{(in)}, \quad (17)$$

$$E_c^{out}(\vec{r}_\perp) \simeq e^{ikn_0 d}[E_c^{(in)}(\vec{r}_\perp) + ikn_1 dE_p^{(in)}], \quad (18)$$

where $J_1^2(2k|n_1|d) \simeq (k|n_1|d)^2$ is the grating diffraction efficiency in the limit of small n_1.

Equations (5), (6), and (14) are the first ingredients of the optical oscillator model. They give the dynamics of the outgoing field $E_c^{(out)}$ as a function of $E_c^{(in)}$. In the following section, we consider the effect of the cavity and evaluate $E_c^{(in)}$ as a function of $E_c^{(out)}$.

In order to illustrate that the LCO can provide an amplification of E_c, we consider the limit $|\bar{n}_1| \ll 1$ and suppose that the incoming field $E_c^{(\text{in})}$ is much slower than n_1. Thus, n_1 follows adiabatically $E_c^{(\text{in})}$ and can be eliminated. Neglecting the spatial derivative in Eq. (6), we have that $n_1 \simeq \alpha E_p^{(\text{in})*} E_c^{(\text{in})}$ and from Eq. (18),

$$E_c^{\text{out}}(\vec{r}_\perp) \simeq e^{ikn_0d}(1 + i\alpha kd|E_p^{(\text{in})}|^2)E_c^{(\text{in})}. \tag{19}$$

Since $|1 + i\alpha kd|E_p^{(\text{in})}|^2| = \sqrt{1 + (\alpha kd)^2|E_p^{(\text{in})}|^4}$ is greater than 1, the LCLV acts as a light amplifier of the field $E_c^{(\text{in})}$. Indeed, from Eq. (19) we derive the usual expression for the 2WM gain in a thin medium [10], that is, $I_c(\text{out})/I_c(\text{in}) = 1 + (\alpha kdI_p)^2$, where $I_c = |E_c|^2$. It is interesting to note an important difference between the LCLV and a photorefractive crystal. In the latter one, α is generally an imaginary number $-i\beta$, thus its amplification factor is $1 + \beta kd|E_p^{(\text{in})}|^2$, i.e., linear in β and for some values smaller than 1. Conversely, in the LCLV the amplification factor is quadratic in α and always greater than 1, as already pointed out in Ref. [10].

B. Field propagation and amplification in the ring cavity

In the preceding section, we have evaluated the outgoing fields from the liquid crystal when two nearly parallel light beams are injected into the LCLV and shown that the device amplifies linearly the weaker field E_c. Now we study the case where this amplifier is inserted in a ring cavity, which reinjects the field $E_c^{(\text{out})}$ into $E_c^{(\text{in})}$. When the cavity losses are smaller than the LCLV gain and for suitable cavity detunings, a spontaneous growth of E_c is triggered by small thermal fluctuations of the refractive index, giving rise to cavity oscillations. In Eq. (14) the field $E_c^{(\text{out})}$ is a function of $E_c^{(\text{in})}$ and n_k. By solving the field equation in the ring, we express the reinjected field $E_c^{(\text{in})}$ as a function of $E_c^{(\text{out})}$, thus eliminating the $E_c^{(\text{out})}$ dependence in Eq. (14) and closing the model.

We assume $E_p^{(\text{in})}$ constant in space and time. The cavity field in vacuum satisfies the equation

$$\left(\nabla^2 - \frac{1}{c^2}\frac{\partial^2}{\partial t^2}\right)E_c(\vec{r}, t)e^{i(\vec{k}_c \cdot \vec{r} - \omega_p t)} = 0. \tag{20}$$

The carrier must be a continuous function along the ring, thus

$$|\vec{k}_c|(L_{\text{cav}} - d) + \tilde{n}|\vec{k}_c|d = 2\pi N, \tag{21}$$

where N is an integer number to be chosen in such a way that the condition $|\vec{k}_c| \simeq k = \omega_p/c$ is satisfied. Note that $\tilde{n}$ is the uniform refractive index, which depends on the working point of the LCLV through the applied voltage V_0 and the input pump intensity I_p.

If the loss rate is much larger than $1/\tau$, we can use also in this case the adiabatic approximation and neglect the time derivative of E_c. In the paraxial approximation we neglect the second derivative in z of E_c and have

$$\frac{\partial E_c(\vec{r})}{\partial z} = \left(\frac{i}{2k}\nabla_\perp^2 + i\Delta\omega/c\right)E_c(\vec{r}), \tag{22}$$

where $\Delta\omega \equiv \omega_p - c|\vec{k}_c|$ is the frequency detuning of the E_c carrier with respect to the pump and depends on E_p by means of $\tilde{n}$. By linearizing Eq. (21) we have

$$\Delta\omega = \Delta\omega_c + \tilde{n}\frac{\omega_p d}{L_{\text{cav}}}, \tag{23}$$

where $\Delta\omega_c$ depends on the cavity configuration and the second term is the contribution of the uniform refractive index $\tilde{n} = n_c + \alpha|E_p^{(\text{in})}|^2$.

The evolution operator through a distance L is

$$e^{i\Delta\omega L/c}\hat{A}(L) \equiv e^{(iL/2k)\nabla_\perp^2 + (i\Delta\omega L/c)}. \tag{24}$$

In analogy with quantum mechanics, we define an operator which describes the field evolution when it passes through the lens. The vacuum evolution operator $\frac{i}{2k}\nabla_\perp^2$ is analogous to the inertial operator of a nonrelativistic particle, which corresponds classically to the Hamiltonian $\frac{1}{2k}\vec{p}_\perp^2$. This classical limit is equivalent to the geometrical optics limit of the Maxwell equations. A ray can be considered as the trajectory of a particle with momentum $\vec{p}_\perp$ and transverse coordinate $\vec{r}_\perp$. In our case, z corresponds to time. For rays parallel to the cavity axis, $\vec{p}_\perp$ is zero. The corresponding equations of motion are

$$\frac{d\vec{r}_\perp}{dz} = \frac{1}{k}\vec{p}_\perp, \tag{25}$$

$$\frac{d\vec{p}_\perp}{dz} = 0. \tag{26}$$

Their integration from $z = z_0$ to z_1 gives linear equations whose coefficients are the *ABCD* matrix elements of the ray transfer matrix [12]

$$\begin{pmatrix} 1 & (z_1 - z_0)/k \\ 0 & 1 \end{pmatrix} \tag{27}$$

(here we take the angle between the cavity axis and the ray in rad $\times$ k unit). A lens modifies the direction of rays, i.e., the value of $\vec{p}_\perp$. This effect can be described by the equations

$$\frac{d\vec{r}_\perp}{dz} = 0, \tag{28}$$

$$\frac{d\vec{p}_\perp}{dz} = -\beta\vec{r}_\perp, \tag{29}$$

integrated over a length d_L. They correspond to the Hamiltonian $\beta r_\perp^2/2$. Since parallel rays are focused at the focal distance f, we find that $d_L\beta = k/f$. Thus, the field evolution through the lens is described by the operator

$$\hat{B}(f) \equiv e^{(-ik/2f)r_\perp^2}, \tag{30}$$

apart from an unimportant phase factor.

The overall evolution operator through the ring cavity is

$$\hat{C} \equiv \Gamma^{1/2} e^{i\delta} \hat{S}^{s_m} \hat{A}(L_{\text{cav}} - L_1) \hat{B}(f) \hat{A}(L_1), \qquad (31)$$

where L_1 is the distance between the LCLV and the lens, $(1-\Gamma)$ is the fraction of lost photons in a round trip, and $\hat{S}$ is the specular operator, s_m being the number of mirrors of the cavity. $\hat{S}$ exchanges $\vec{r}_\perp$ with $-\vec{r}_\perp$ and obviously commutes with $\hat{A}$ and $\hat{B}$. The phase detuning δ depends on $\tilde{n}$ as [see Eq. (23)]

$$\delta = \delta_c + kd\tilde{n}, \qquad (32)$$

where δ_c is set by the cavity. The field $E_c^{(\text{out})}$ evolves through a round trip to $\hat{C}E_c^{(\text{out})} = E_c^{(\text{in})}$, and from Eq. (14) we obtain the equality

$$\hat{C}e^{i\bar{n}_0}\left[J_0(2|\bar{n}_1|)E_c^{(\text{in})} + i\frac{\bar{n}_1}{|\bar{n}_1|}J_1(2|\bar{n}_1|)E_p^{(\text{in})} \right] = E_c^{(\text{in})}, \quad (33)$$

with $\hat{C}$ the cavity operator defined in Eq. (31). When solving for E_c, we obtain

$$(1 - \hat{D})E_c^{(\text{in})}(\vec{r}_\perp) = \hat{G}E_p^{(\text{in})}, \qquad (34)$$

where

$$\hat{D} \equiv \hat{C}e^{i\bar{n}_0}J_0(2|\bar{n}_1|) \qquad (35)$$

is the operator describing the mutual coupling between the cavity modes, accounting also for losses due to scattering out of the cavity axis, and

$$\hat{G} \equiv \hat{C}e^{i\bar{n}_0}\frac{i\bar{n}_1}{|\bar{n}_1|}J_1(2|\bar{n}_1|) \qquad (36)$$

is the operator accounting for the two-wave mixing process of photon injection inside the cavity. Since the eigenvalues of $\hat{D}$ are complex numbers with modulus smaller than 1, $(1-\hat{D})^{-1}$ can be written as a Taylor series, then we have the following solution for $E_c^{(\text{in})}$:

$$E_c^{(\text{in})}(\vec{r}_\perp) = \sum_{s=0}^{\infty} \hat{D}^s \hat{G}E_p^{(\text{in})}. \qquad (37)$$

Equations (5), (6), and (37) constitute our model. The first two equations describe the dynamics of n_0 and n_1 and contain the cavity field $E_c^{(\text{in})}$, given by the last equation as function of the refractive indices. Equation (37) has a simple physical interpretation. The first term with $s=0$ gives the field scattered by the liquid crystal into the cavity with $E_c^{(\text{in})}=0$ and its subsequent evolution through a round trip. The other terms are the contribution of this field after s returns to the LCLV. Because of the cavity losses, this series converges and can be approximated by a finite number of terms. The relative error with N terms is of the order of $\Gamma^{N/2}$, thus with $\Gamma=0.8$ and 40 iterations the relative error is about 1%. In Appendix A we show that it can be further reduced when the value of $E_c^{(\text{in})}(t-dt)$ at the previous time $t-dt$ is used as an estimate of $E_c^{(\text{in})}(t)$. The evolution given by the cavity operator $\hat{C}$ can be numerically implemented by means of fast Fourier transforms.

Note that the thickness of the liquid crystal layer is a parameter of the model. With the rescaling of the refractive indices $kdn_l \rightarrow \bar{n}_l$, it can be absorbed by $\bar{\alpha}$, defined as

$$\bar{\alpha} = kd\alpha. \qquad (38)$$

In this way, we have eliminated in Eq. (37) the dependence on d.

IV. ANALYSIS OF THE MODEL

In the linear regime the cavity field grows exponentially above a threshold value of the pump intensity, until saturation terms become relevant. In Sec. IV A we analyze the model for the LCO in the one-mode approximation evaluating the threshold value and identifying the saturation mechanisms. In Sec. IV C we recover the familiar mean-field equations under suitable conditions.

A. One-mode approximation

We assume that only one longitudinal, one transverse mode of the cavity is nearly resonant and undergoes oscillations. This condition can be experimentally obtained by setting a diaphragm inside the cavity and by closing it in such a way that only the fundamental transverse mode is selected. The selection of the longitudinal mode takes place through the frequency detuning with respect to the pump field, as it follows from the analysis below. In the one-mode approximation the operator equation (34) is replaced by the scalar one

$$E_c^{(\text{in})} = \frac{i\bar{n}_1}{|\bar{n}_1|}\frac{\Gamma^{1/2}e^{i(\delta_0+\bar{n}_0)}J_1(2|\bar{n}_1|)}{1 - \Gamma^{1/2}e^{i(\delta_0+\bar{n}_0)}J_0(2|\bar{n}_1|)}E_p^{(\text{in})}, \qquad (39)$$

where δ_0 is the phase acquired by the cavity field in a round trip, i.e., $\delta_0 c/L_{\text{cav}} \equiv \omega_0$ is the frequency detuning of the cavity mode with respect to the pump field. Let us assume that the eigenmode is smooth with respect to the diffusion length l_0 and neglect the derivative terms in Eqs. (5) and (6), which become

$$\tau\frac{\bar{n}_0}{dt} = -\bar{n}_0 + \bar{\alpha}|E_c^{(\text{in})}|^2, \qquad (40)$$

$$\tau\frac{\bar{n}_1}{dt} = -c_1\bar{n}_1 + \bar{\alpha}E_p^{(\text{in})*}E_c^{(\text{in})}. \qquad (41)$$

We now linearize Eqs. (40) and (41), in order to study the stability of the stationary solution $\bar{n}_0 = \bar{n}_1 = 0$ and find the threshold condition for the cavity oscillation. The first equation gives $\tau d\bar{n}_0/dt = -\bar{n}_0$, thus we can take $\bar{n}_0 = 0$ and consider only the second equation, which yields

$$\tau\frac{\bar{n}_1}{dt} = \left(-c_1 + \bar{\alpha}I_p\frac{i\Gamma^{1/2}e^{i\delta_0}}{1 - \Gamma^{1/2}e^{i\delta_0}} \right)\bar{n}_1 \equiv c_2\bar{n}_1. \qquad (42)$$

The threshold condition is $\text{Re}[c_2] > 0$, i.e.,

$$-c_1 - \bar{\alpha}I_p\frac{\sin\delta_0}{1 + \Gamma - 2\Gamma^{1/2}\cos\delta_0} > 0. \qquad (43)$$

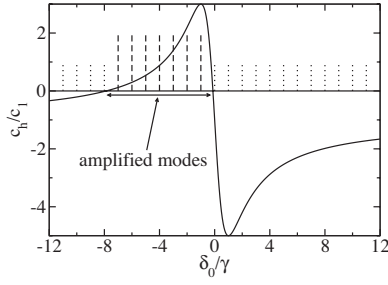The second term is an odd function of δ_0, is zero at $\delta_0 = 0$, and has a maximum at

FIG. 3. c_h/c_1 as a function of δ_0/γ for $\bar{\alpha}I_p/\gamma c_1 = 8$. The dashed lines represent the amplified modes of the cavity. The dotted lines are the subthreshold ones. Note that $\bar{\alpha}$ is taken positive. For $\bar{\alpha} < 0$, the δ_0/γ axis is reversed.

$$\delta_0^M = -\,\mathrm{sgn}(\bar{\alpha})\,\mathrm{asin}\frac{1-\Gamma}{1+\Gamma}. \tag{44}$$

With $\delta_0 = \delta_0^M$, the threshold value of $\bar{\alpha}I_p$ is minimal and given by

$$|\bar{\alpha}|I_p^{\mathrm{thr}} = \frac{1-\Gamma}{\Gamma^{1/2}}c_1. \tag{45}$$

As noted in Sec. III A, α is imaginary in photorefractive crystals, thus the real part of c_2 is even and has a maximum at $\delta_0 = 0$. Conversely, in LCLV the overall gain is always negative for $\delta_0 = 0$, since there is a phase mismatch between the triggering grating n_1 and the grating generated by the feedback field. With regard to this consideration, note that in Eq. (19) the outgoing field $E_c^{(\mathrm{out})}$ is equal to the incoming one plus a contribution with phase detuning $\pi/2$, when $n_0 = 0$.

For cavities with very small losses, δ_0^M is much smaller than 1, thus for I_p of the order of I_p^{thr} the threshold condition becomes

$$\frac{c_h}{c_1} \equiv -1 - \frac{\bar{\alpha}I_p}{c_1}\frac{\delta_0}{\gamma^2+\delta_0^2} > 0, \tag{46}$$

where $\gamma \equiv 1-\Gamma^{1/2} \ll 1$. In Fig. 3 we report c_h/c_1 as a function of δ_0/γ for $\bar{\alpha}I_p/\gamma c_1 = 8$. The dashed lines represent the resonant modes and have a negative δ_0, whereas the dotted lines are the subthreshold modes. For high negative detuning the gain decreases and becomes negative, because of the phase mismatch among the cavity fields with different number of round trips [in other words, the terms in the series of Eq. (37) sum up to zero because of destructive interference effects].

It is interesting to note that the imaginary part of c_2 gives a phase rotation of $\bar{n}_1$ and, consequently, of E_c. Thus, the cavity field has a phase drift with respect to the pump E_p. The corresponding frequency difference, called *pulling* [13], is always negative and for $\gamma \ll 1$ equal to

$$\omega_{\mathrm{pull}} = -\frac{1}{\tau}\frac{\bar{\alpha}I_p\gamma}{\gamma^2+\delta_0^2}. \tag{47}$$

At the threshold and for $\delta_0 = \delta_0^M$,

$$|\omega_{\mathrm{pull}}^{\mathrm{thr}}| \sim \frac{c_1}{2\tau}, \tag{48}$$

i.e., it is of the order of the relaxation rate of n_1.

The complex variable $\bar{n}_1$ can be specified by its real amplitude $\bar{n}_A$ and phase ϕ_1, as follows:

$$\bar{n}_1 \equiv \bar{n}_A e^{i\phi_1}. \tag{49}$$

The evolution of $\bar{n}_A$ and $\bar{n}_0$ is independent of ϕ_1, thus the one-mode system is fully described by only two variables. For a higher number of modes, in general the phases cannot be eliminated. When many modes are simultaneously oscillating in the cavity, the phase dynamics may become very complex and can lead to the formation of spatiotemporal pulses confined in the three space directions, as we will see later.

B. Saturation and nonlinear effects

In the linear regime and above threshold, the cavity field grows exponentially until saturation becomes relevant. There are two mechanisms for saturation: (1) the change of the detuning, carried out by the slow evolution of n_0, (2) the pump depletion, due to the multiple scatterings of the pump beam (see Fig. 2).

As we will show in Sec. V, the first mechanism is dominant when δ_0 is sufficiently small. In this analysis the sign of $\bar{\alpha}$ is not important, however for the sake of simplicity we assume it to be negative, as occurs in the LCLV. When the cavity field increases, $\bar{n}_0$ undergoes a negative drift [Eq. (40)]. We have shown that in the linear regime the gain is sensitive to the phase δ_0. If the nonlinear terms are retained, the overall phase shift after a round trip is $\delta_0 + \bar{n}_0$, according to Eq. (39). Thus the effect of $\bar{n}_0$ is to drift the phase and to reduce the amplification factor $\mathrm{Re}(c_2)$, until it becomes negative and $\bar{n}_1$ begins to decrease. For different values of the parameters, the system can undergo oscillations or relax toward a stationary state.

The pump depletion provides another mechanism of saturation. The function J_0 is decreasing for small $|\bar{n}_1|$ and in this range J_1 is convex, thus the amplification factor is further reduced by multiscattering processes and pump depletion, as expected. We neglect these extra contributions and assume that $J_0(2|\bar{n}_1|) \simeq 1$ and $(\bar{n}_1/|\bar{n}_1|)J_1(2|\bar{n}_1|) \simeq \bar{n}_1$. With these approximations, we have from Eqs. (39)–(41) that

$$\tau\frac{\bar{n}_0}{dt} = -n_0 + \frac{\bar{\alpha}I_p\Gamma n_A^2}{1+\Gamma-2\Gamma^{1/2}\cos(\delta_0+\bar{n}_0)}, \tag{50}$$

$$\tau\frac{\bar{n}_A}{dt} = \left(-c_1 - \frac{\bar{\alpha}I_p\Gamma^{1/2}\sin(\delta_0+\bar{n}_0)}{1+\Gamma-2\Gamma^{1/2}\cos(\delta_0+\bar{n}_0)}\right)\bar{n}_A. \tag{51}$$

The state $\bar{n}_A = \bar{n}_0 = 0$ is a stationary solution. Other stationary states must satisfy the equations

$$-\frac{\bar{\alpha}I_p}{c_1} = \frac{1}{\Gamma^{1/2}}\frac{1+\Gamma-2\Gamma^{1/2}\cos(\delta_0+\bar{n}_0)}{\sin(\delta_0+\bar{n}_0)} \equiv \mathcal{G}(\delta_0+\bar{n}_0), \tag{52}$$
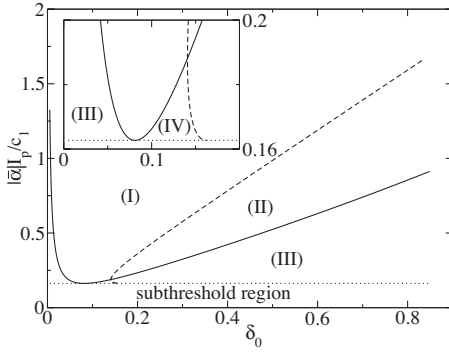
FIG. 4. Phase diagram in δ_0 and $|\bar{\alpha}|I_p/c_1$, for $\bar{\alpha}<0$. The zero field configuration is the only stationary solution below the dotted line, whereas two additional solutions are present above it. Above the continuous line the zero field solution becomes unstable. At the left of the dashed line, one of the two additional solutions is stable, whereas the other one is always a saddle node. The inset shows a magnification of the bistable region (IV) close to threshold.

$$\bar{n}_A^2 = -\frac{\sin(\delta_0 + \bar{n}_0)\bar{n}_0}{c_1 \Gamma^{1/2}}. \tag{53}$$

In Fig. 4 we report the phase diagram in δ_0 and $|\bar{\alpha}|I_p/c_1$, for $\bar{\alpha}<0$ and $\Gamma=0.85$. The continuous curve represents the solutions of Eq. (52) for $\bar{n}_0=0$ and above it the zero field state is unstable, as previously shown. The minimum is at $\delta_0 = \delta_0^M$ and takes the value $|\bar{\alpha}|I_p^{\text{thr}}/c_1$. δ_0^M and I_p^{thr} are defined by Eqs. (44) and (45), respectively. It is clear that Eqs. (52) and (53) have two solutions when $I_p > I_p^{\text{thr}}$. Conversely, no solution exists if $I_p < I_p^{\text{thr}}$ and the system decays always towards the zero cavity field state. This case corresponds to the subthreshold region below the dotted line in Fig. 4. Note that by changing the value of Γ the boundaries between the different regions can be modified, however, the existence of the regions remains unaffected.

We determine the stability conditions for the two nonzero stationary states above the threshold I_p^{thr}. We linearize Eqs. (50) and (51) around the two stationary solutions and find the eigenvalues

$$\lambda_\pm = -\frac{\bar{B}}{2\tau\bar{A}} \pm \frac{\sqrt{\bar{B}^2 + 4\bar{A}\bar{n}_0 c_1[4c_1 + 2\bar{A}\cot(\delta_0 + \bar{n}_0)]}}{2\tau\bar{A}}, \tag{54}$$

where $\bar{A} \equiv \bar{\alpha}I_p < 0$ and $\bar{B} \equiv \bar{A} - 2c_1\bar{n}_0$. $\bar{n}_0$ is one of the two nonzero solutions of Eq. (52). The product $\bar{A}\bar{n}_0$ being positive, the stability condition $\mathrm{Re}[\lambda_\pm] < 0$ is satisfied if

$$\bar{A} - 2c_1\bar{n}_0 < 0,$$

$$4c_1 + 2\bar{A}\cot(\delta_0 + \bar{n}_0) < 0. \tag{55}$$

The second inequality is satisfied if and only if $0 < \delta_0 + \bar{n}_0 < \delta_0^M$. Thus, the solution with higher overall phase shift is always a saddle node. The other one is stable if the first inequality is satisfied. The values of $|\bar{\alpha}|I_p/c_1$ and δ_0 with $\bar{A} - 2c_1\bar{n}_0 = 0$ are given by the following parametric equations:

$$\delta_0 = q + \mathcal{G}(q)/2, \qquad 0 < q < \delta_0^M, \tag{56}$$
$$|\bar{\alpha}|I_p^{\text{thr}}/c_1 = \mathcal{G}(q),$$

and they are represented by the dashed line in Fig. 4. Above it the system has a stable solution with nonzero cavity field. Thus, we have identified five distinct regions. The subthreshold region is below the dotted line, where only the zero field solution is stationary and every trajectory moves towards it. The (I–IV) regions are characterized by two additional stationary states with nonzero field; one of them is always a saddle node. In region I the other state is stable and the zero field configuration is unstable. In region II there is no stable solution and the system has a stable limit cycle. The transition from region I to region II takes place through a Hopf bifurcation. In region III only the zero field is a stable solution. However, it is possible that in a subset of this region the system has a stable limit cycle, as shown in Sec. V. In this case we have a bistability between a fixed point and a limit cycle. In region IV the system is bistable with two stable fixed points. These different situations will be studied numerically in Sec. V, where we will consider also the multiscattering processes and pump depletion.

C. Mean-field approximation

In the preceding section we have shown that near threshold the activated modes have a frequency detuning ω_0 in a narrow interval around γ/t_c, $t_c \equiv L_{\text{cav}}/c$ being the cavity round-trip time. In this section we set the system in this interval and obtain under suitable conditions the mean-field equations.

In Appendix B, we evaluate the frequencies of the cavity modes, that are [Eq. (B13)]

$$\Omega_{p,q,l} = \omega_\perp(p+q) + \omega_\| l, \tag{57}$$

where $\omega_\perp$ and $\omega_\|$ are the frequency spacings of the transverse and longitudinal modes, respectively, and p, q, l are nonnegative integer numbers.

The phase factor of a cavity eigenmode after a round trip is [see Eq. (31) and (B12)]

$$F_{\text{rt}} \equiv e^{-i\omega_\perp(p+q)t_c + i\delta}, \tag{58}$$

where δ is given by Eq. (32). In Sec. IV A, we have seen that slightly above threshold only the modes which have

$$F_{\text{rt}} \simeq e^{-i\gamma_c t_c/2} \tag{59}$$

are activated. If $\gamma_c t_c \ll 1$, this implies that $|[\omega_\perp(p+q)t_c - \delta]\mod 2\pi| \ll 1$. If the 2WM device has a sufficiently small transverse dimension, only the transverse modes with small p and q are activated, thus

$$|\omega_\perp(p+q)t_c - \delta| \ll 1, \tag{60}$$

once we assume $|\delta| \ll 2\pi$. In the limit of $kd|n_{0,1}| \ll 1$, we have the following approximation for $\hat{D}$:
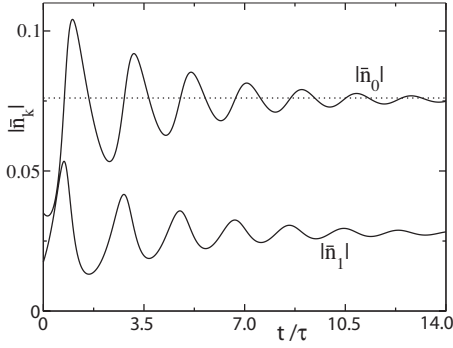
FIG. 5. $|\bar{n}_0|$ and $|\bar{n}_1|$ as functions of time for $\bar{\alpha}I_p/c_1=0.3$ and $\delta_0=0.1$ (region I of Fig. 4).

$$\hat{D} \simeq 1 - \frac{\gamma_c L_{\text{cav}}}{2c} + i\delta - \frac{iC_d t_c}{2}\nabla_\perp^2 + \frac{iC_l t_c}{2}r_\perp^2 + ikdn_0, \quad (61)$$

where C_d and C_l are defined in Appendix B. Similarly, we approximate $\hat{G}$ with $ikdn_1$ and obtain from Eq. (34) the following:

$$\left(-\frac{\gamma_c L_{\text{cav}}}{2c} + i\delta - \frac{iC_d t_c}{2}\nabla_\perp^2 + \frac{iC_l t_c}{2}r_\perp^2 + ikdn_0\right)E_c = -ikdn_1 E_p.$$
$$(62)$$

In the limit of $f \to \infty$, we have (Appendix B)

$$\left[\frac{ic^2}{2\omega_p}\nabla_\perp^2 + \left(i\frac{\delta c}{L_{\text{cav}}} - \frac{\gamma_c}{2}\right) + i\frac{\omega_p d}{L}n_0\right]E_c = -i\frac{\omega_p d}{L}n_1 E_p,$$
$$(63)$$

which is the time-independent equation of the cavity field in the mean-field approximation and for a plane cavity [6]. It is clear that this approximation is broken when the nonlinear medium has a large transverse dimension and the approximation of Eq. (60) is no more appropriate.

V. NUMERICAL SIMULATIONS

In this section we report some numerical simulations of the LCO model. In Sec V A we integrate the one-mode equations (50) and (51) and consider the (I–IV) regions, identified in the preceding section. In Sec V B we study the multimode case and show that the interference among the cavity modes generates spatiotemporal pulses.

A. One-mode simulations

In the simulations of the one-mode system we have fixed the following parameters: $\tau=0.15$ s, $\Gamma=0.85$, and $c_1=2.58$. In Fig. 5 we report the dynamics of $|\bar{n}_0|$ and $|\bar{n}_1|$ for $\bar{\alpha}I_p/c_1 =0.3$ and $\delta_0=0.1$ (region I). The dotted line is the stationary value of $\bar{n}_0$. Note that $|\bar{n}_1|$ reaches the local maxima when $|\bar{n}_0|$ crosses the dotted line, i.e., when the coefficient on the right-hand side of Eq. (51) is zero. During the transient time the refractive indices undergo damped oscillations around the stationary state. This implies that the argument of the
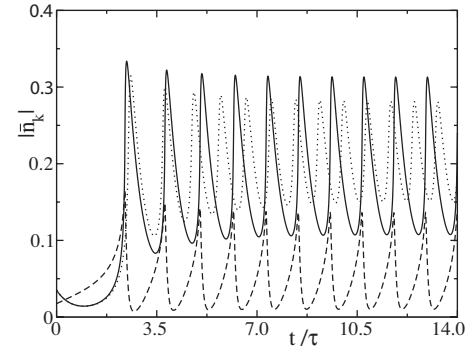

FIG. 6. The same as Fig. 5, but with $\delta_0=0.25$ (region II). The solid and dashed lines are $|\bar{n}_0|$ and $|\bar{n}_1|$. The dotted line is $\bar{n}_0$, evaluated including the Bessel functions in the dynamical equations.

square root in Eq. (54) is negative and the eigenvalues $\lambda_\pm$ are complex with the real part negative.

For smaller δ_0 and I_p we observe that $\bar{n}_0$ collapses towards its stationary value without oscillations. In this case the argument of the square root is positive and the eigenvalues are real and negative. This occurs, for example, with $\delta_0=0.05$ and $\bar{\alpha}I_p/c_1=0.19$.

Figure 6 is the same as Fig. 5, but with $\delta_0=0.25$ (region II). The solid and dashed lines are $|\bar{n}_0|$ and $|\bar{n}_1|$, respectively. In this case there is no stable point and the dynamics becomes oscillatory after a transient time. Note that $\bar{n}_1$ has maxima of the order of 0.15, thus the multiscatterings and pump depletion give relevant contributions. The dotted line is $\bar{n}_0$, evaluated including the Bessel functions in the dynamical equations. With this correction there is still a stable limit cycle, but the oscillation amplitude is smaller.

In the preceding section we have shown that in region III only the state with zero field is a stable stationary state. However, for some values of the parameters this state coexists with a stable limit cycle. In Fig. 7(a) we report $|\bar{n}_1|$ as a function of time for $\bar{\alpha}I_p/c_1=0.21$ and $\delta_0=0.2$ (region III). At the initial time, $|\bar{n}_1|$ is zero and stable. At a subsequent time a small pulse with Gaussian temporal shape is added to the pump field, centered at $t=5$ s and with the standard deviation
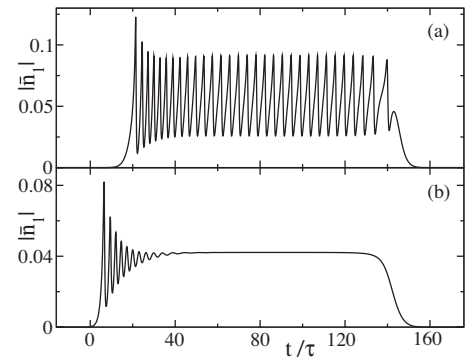

FIG. 7. $|\bar{n}_1|$ as a function of time, for $\bar{\alpha}I_p/c_1=0.21$, $\delta_0=0.2$ (a) and $\bar{\alpha}I_p/c_1=0.17$, $\delta_0=0.13$ (b). In both cases a positive pulse and a negative one are added to the pump at $t=5$ and 27 s, respectively. In (a) (region III) we have bistability between a stable fixed point and a limit cycle. In (b) (region IV) there are two stable fixed point.

equal to about 0.1 s. The peak intensity variation is about 30% of I_p and is sufficient to make the zero field state unstable. This pulse carries the system into the stable limit cycle. Finally a dark pulse of the pump field is generated at $t=22$ s and the system goes into the original state. This simulation has been performed including the multiscatterings and the pump depletion. An identical behavior is obtained also with the approximate equations (50) and (51).

In region IV the system has two stable fixed points, as shown in Fig. 7(b). Also in this case we have added a positive and negative pulse to the pump field at different times, but with $\bar{\alpha}I_p/c_1=17$ and $\delta_0=0.13$. After the first pulse the system goes into the stable state with $\bar{n}_1 \neq 0$. After the second pulse, it returns into the original state. Also, for this simulation we have used in the equations the Bessel functions. They slightly change the dynamics, but the qualitative behavior remains unchanged.

We have shown numerically the existence of different dynamical regimes, as identified in Sec. IV by means of Eqs. (50) and (51). The more precise inclusion of multiscatterings and pump depletion effects change quantitatively the dynamics and distort the boundaries of the regions in Fig. 4, mainly for high δ_0, but the different regimes do not disappear. It is evident that the corrections are more relevant when δ_0 is larger, since $\bar{n}_0$ tends to counterbalance δ_0 so as to carry the overall phase shift $\delta_0+\bar{n}_0$ to the value $\mathcal{G}^{-1}(|\bar{\alpha}|I_p/c_1)$ [Eq. (52)], where the inverse of $\mathcal{G}$ is defined taking into consideration only the left branch of the continuous curve in Fig. 4. Note that the argument of the Bessel functions contains $|\bar{n}_1|$, which increases by increasing $\bar{n}_0$ [Eq. (53)].

B. Multimode simulations

We consider the multimode theory previously introduced for the configuration of the experiment discussed in the next section. For the sake of simplicity, we study the case with one transverse dimension. The cavity has a length $L_{cav}=240$ cm, it is composed of three mirrors ($s_m=3$) and a lens with focal length $f=70$ cm. The pump beam is generated by a diode pumped solid state laser ($\lambda=532$ nm) with an intensity of about 2 mW/cm^2. The liquid crystal thickness d is equal to 15 μm. We assume that the fraction of lost photons in a round trip is 25%, i.e., $\Gamma=0.75$, and set $c_1=5.5$, $l_0=3 \times 10^{-2}$, and $\tau=0.15$ s.

The frequency spacing of the transverse modes is given by Eq. (B11) and in our case we have $\omega_\perp=96.9 \times 10^6$ s^{-1}. If $L_1=L_{cav}/2$ and the liquid crystal is in the waist of the cavity, the eigenstates of the operator $\hat{C}$ in Eq. (31) are the Hermite functions $\bar{\mathcal{E}}_n(x)=H_n(c_sx)e^{-(c_s^2x^2/2)}$, where $c_s \equiv (C_d/C_l)^{1/4}$, C_d and C_l being defined in Appendix B. If $L_1 \neq L_{cav}/2$, the eigenstate is the evolved field $\mathcal{E}_n \equiv e^{-(i/2k)(L_1-L_{cav}/2)\nabla_\perp^2}\bar{\mathcal{E}}_n$. The corresponding phase shift after a round trip is $\delta_n \equiv \delta_{ho}(1/2+n)-\pi/2+\delta$, where $\delta_{ho} \equiv \omega_\perp L_{cav}/c=0.775$ rad.

We have shown that a single mode can display different dynamical regimes, depending on the phase shift of the field after a round trip and on the pump intensity. The mode with phase shift equal to δ_0^M has the maximal gain. If we set $\delta=\delta_0^M+\pi/2-\delta_{ho}(1/2+N_0)$, where N_0 is an integer number,
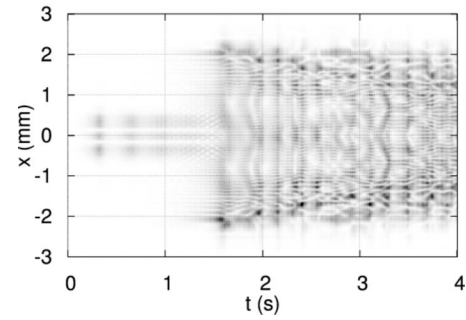

FIG. 8. Spatiotemporal intensity distribution of the cavity field $|E_c^{(in)}|^2$ for $\delta=\delta_0^M+\pi/2-\delta_{ho}(1/2+2)$ and $I_p=1.5I_p^{thr}$.

and the pump intensity is not too high, only the cavity mode N_0 is triggered. In Fig. 8, we report the spatiotemporal distribution of the cavity field intensity $|E_c^{(in)}|^2$, for $N_0=2$ and $I_p=1.5I_p^{thr}$. At the initial time the mode $\mathcal{E}_2$ grows and has damped oscillations around a stationary nonzero value, as it occurs in the one-mode case of Fig. 5. After a transient time, higher modes are activated and a complex spatiotemporal structure appears.

In order to clarify this behavior, we have decomposed the cavity field in eigenmodes and evaluated the mode amplitudes as a function of time. In Fig. 9 we report the squared amplitudes of the cavity modes as a function of time. At the initial times, only the mode 2 is dominant, subsequently its amplitude decreases and seven other modes are activated. Because of the large value of δ_{ho} with respect to γ, adjacent modes cannot be simultaneously activated, but this is possible for modes whose index distance is equal to 8, the corresponding phase shift difference being $8\delta_{ho} \simeq 0.987 \times 2\pi$. Note that the modes 51 and 59 are the first activated ones, since the phase shift distance from the mode 2 is smaller than that of the lower modes. The higher modes are suppressed because of the spatial diaphragms inside the cavity. It is interesting to note that the jump from the low mode 2 to the higher ones is triggered by the growing $\bar{n}_0$, which modifies the cavity detuning. This is another peculiarity of the LCLV with respect to photorefractive crystals.

From Fig. 9 we see that there are eight predominant modes, corresponding to the high intensity bands on the plot. However, in the graph are plotted the square amplitudes of the modes, so that even the modes represented by low levels
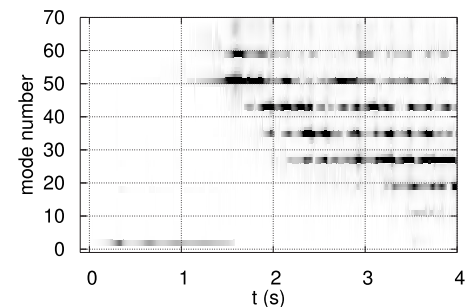

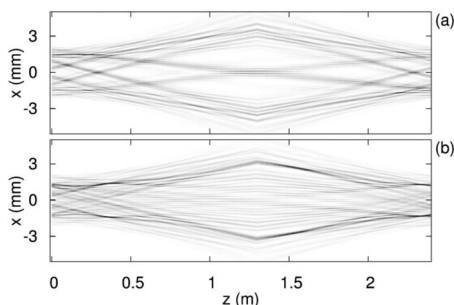FIG. 9. Squared amplitudes of the cavity modes for the dynamics of Fig. 8.

FIG. 10. Intensity distribution of the cavity field in the x-z plane at $t=3.5$ s (a) and $t=4$ s (b). Because of the activation of high order modes, the field is inomogeneous along z and a mean-field approximation along the cavity axis is unsuitable. The lens is positioned at $z=1.3$ m.

of intensity cannot be neglected and they indeed participate to the dynamics. Thus, the total number of active modes is approximately 60. An extension to a two-dimensional (2D) model will lead to approximately 3600 active modes, which is consistent with the huge number of modes observed in the experiment.

These results clearly show that our model accounts in a natural way for longitudinal modes and that the mean-field approximation is inappropriate to describe the considered system. It is valid when the phase shift differences of the active modes are much smaller than 2π. The breakdown of the mean-field approximation is due to both the particular geometry of the cavity and the large transverse dimension of the LCLV. Its consequence is a pattern structure of the cavity field along the z axis, as shown in Fig. 10, where we report the intensity distribution of the cavity field in the x-z plane. Two movies of the dynamics in the x-z plane are available [8]. The simulations in files "theory_1.mp4" and "theory_2.mp4" have been performed for $E_p=7E_p^{thr}$ and $E_p=5E_p^{thr}$, respectively.

VI. EXPERIMENTAL RESULTS

The experiments were performed by using the setup shown in Fig. 1. In Fig. 11 we show a sequence of instantaneous snapshots of the transverse intensity distributions $I_c(x,y)$, where x,y are the coordinates in the transverse plane, taken for a low Fresnel number, $F=3$, when the cavity field consists of a small number of transverse modes around a single longitudinal mode. A few low-order Gauss-Laguerre modes alternate during the time. This behavior is similar to
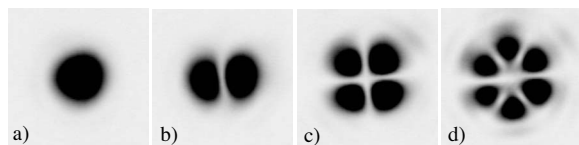

FIG. 11. Instantaneous snapshots showing the low-order Gauss-Laguerre modes alternating during the time for $F=3$; (a) TEM_{00}, (b) TEM_{10}, (c) TEM_{11}, (d) TEM_{06}.
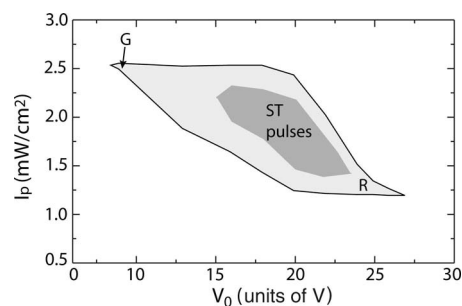

FIG. 12. Experimental phase diagram in the V_0 versus I_p space; G indicates the zone of low-order Gaussian modes whereas R marks the region of wide ring patterns.

dynamical regimes previously observed in photorefractive oscillators [3]. In our model, the alternation between modes is explained by the δ_0 shift due to the dynamics of n_0. Following the slow evolution of n_0, each single mode lasts for a few seconds before changing to another one. Depending on the control parameters, namely, the voltage V_0 applied to the light valve and the pump intensity I_p, the alternation may be periodic or chaotic.

In the single mode regime, we have measured the frequency detuning between the pump and the cavity field. This is done by making the interference of the cavity field with a reference beam having the same frequency of the pump. The displacement of the interference fringes corresponds to a detuning, of approximately 1 Hz, which is the same for the different transverse modes and corresponds to the pulling predicted by Eq. (48).

In a second series of experiments, we have fixed a large Fresnel number $F=500$, and we have investigated the dynamical behavior of the cavity for different V_0 and different pump intensities I_p. The experimental phase diagram is reported in Fig. 12. Cavity field oscillations are in the larger grey area. The darker and smaller area marks the region where we observe spatiotemporal pulses [4]. The low V_0 regimes are similar to those observed for low F, characterized by the alternation of low-order Gauss-Laguerre modes, one pure mode at time. By changing V_0 we change the uniform refractive index of the LCLV, thus the frequency detuning between the fundamental Gaussian mode and the pump field is varied. When V_0 increases, the detuning also increases, therefore out-of-axis emission is favored and a larger number of modes comes into play [14]. As a consequence, the transition to the high V_0 regimes is accompanied by the emission of high order and out-of-axis symmetrical modes.

In Fig. 13 we show a regime where an intermediate number of modes are active. The cavity field oscillations are characterized by the simultaneous presence of high- and low-order transverse modes, sometimes belonging to different longitudinal modes, as we can verify by making the interference with a reference beam and by observing different fringe displacements in different regions of the spatial pattern. In Fig. 14 we show a regime with a large number of modes but outside the region of existence of spatiotemporal pulses. Figure 14(a) displays a regime of high V_0 and low I_p. In this case the detuning is large, so that wide ring patterns develop
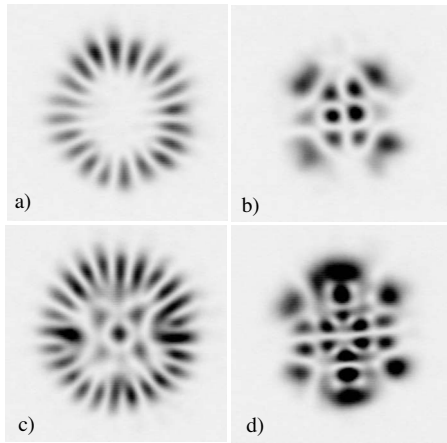
FIG. 13. Instantaneous snapshots taken for an intermediate number of active modes: (a, b) $V_0=10$ V, $I_p=2.4$ mW/cm^2; (c, d) $V_0=14$ V, $I_p=2.0$ mW/cm^2.

with depletion of the oscillations close to the cavity axis. Nevertheless, the number of active modes is large so that a spatiotemporal chaotic dynamics takes place along the ring. Figures 13(b)–13(d) correspond to a slight decrease of V_0, allowing for other longitudinal modes to come into play and populate the central area of the pattern.

For intermediate values of V_0 and I_p, a large number of transverse and longitudinal modes are accepted even close to the cavity axis, thus populating the whole size of the area illuminated by the pump beam. In this regime, we observe the formation of spatiotemporal pulses, appearing as large intensity peaks over a lower amplitude and specklelike background. To investigate the dynamics of spatiotemporal pulses we have fixed $V_0=20.3$ V rms and $I_p=2.0$ mW/cm^2 and we have recorded several movies. The spatiotemporal pulses are identified by applying on each frame a threshold of 3 times the average intensity $\bar{I}_c$ calculated over the entire set of frames in any experimental run.

The extension of the pulses in the z direction is investigated by simultaneously recording the intensity distributions at three different planes, located at z_1, z_2, and z_3 distance with
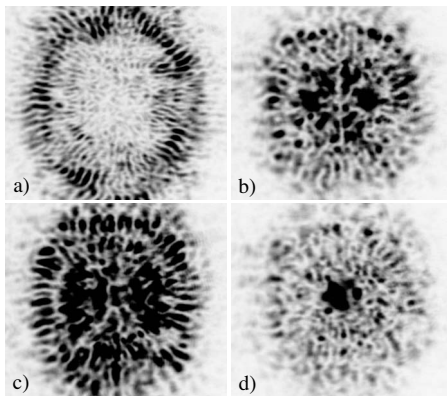

FIG. 14. Instantaneous snapshots taken for a large number of active modes: (a, b) $V_0=25$ V, $I_p=1.3$ mW/cm^2; (c, d) $V_0=23$ V, $I_p=1.3$ mW/cm^2.
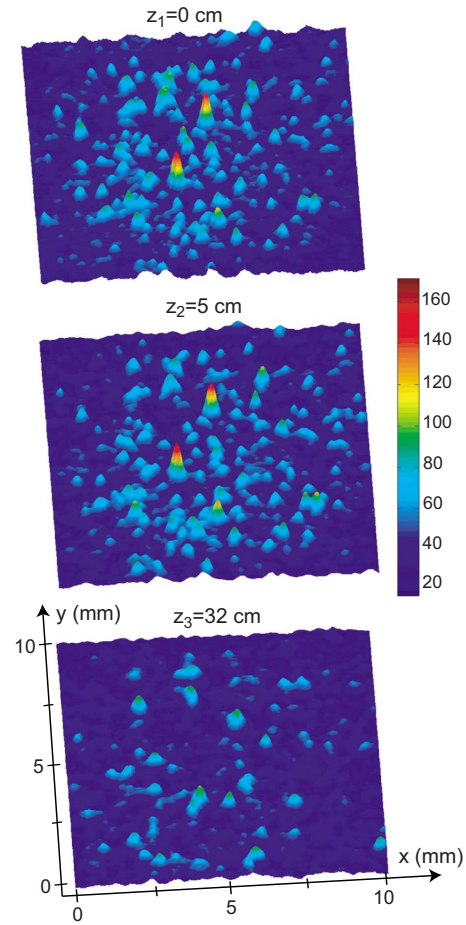

FIG. 15. (Color online) Spatial profiles of spatiotemporal pulses recorded at z_1, z_2, and z_3 for $V_0=20$ V, $I_p=2.0$ mW/cm^2. Colors, from blue (minimal intensity) to red (maximal intensity).

respect to the entrance side of the LCLV. The three CCD cameras recording the movies are driven by the same trigger, whose delay time is negligible with respect to the liquid crystal response time. We select $z_1=0$, $z_2=5$, and $z_3=32$ cm. The magnification ratio, the size of the window and the intensity levels are the same for the three planes.

Three spatial profiles recorded at the three different planes are displayed in Fig. 15. By reslicing the z_2 movie along the direction joining the two pulses, we obtain the spatiotemporal plot shown in Fig. 16. It can be seen from Fig. 15 that at z_3 the two large pulses have disappeared whereas from Fig. 16 we see that the pulses have a limited temporal extension. By taking the half-height width of the pulses with $I_c(x,y,z) > 3\bar{I}_c$ and by averaging over more than 100 profiles, we find that the transverse size of a pulse is 250 ± 50 μm
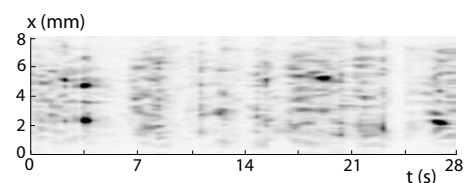

FIG. 16. Spatiotemporal plot obtained from the z_2 movie.

whereas its average lifetime is around 0.5 ± 0.1 s. As for the longitudinal extension, by inspecting several movies taken at different z_3, we estimate it around 30 cm, which is consistent with the results of the 2D numerical simulations.

Three experimental movies are available online [8]. The first movie, recorded for $V_0=10$ V and $I_p=2.4$ mW/cm^2, shows the alternation among a few low-order Gaussian modes, all belonging to the same longitudinal mode. The second movie was recorded for $V_0=14$ V and $I_p=2.0$ mW/cm^2 and shows an increased number of transverse modes corresponding to a few different longitudinal modes. The third movie, recorded for $V_0=20$ V and $I_p=2.0$ mW/cm^2, corresponds to a regime when a high number of transverse and longitudinal modes are simultaneously present.

VII. CONCLUSIONS

In conclusion, we have shown that a type of nonlinear optical oscillator can be built by using a liquid crystal light valve as the gain medium. We have developed a theoretical model that takes into account the Kerr nonlinearity of the medium as well as the two-wave-mixing mechanism of photon injection inside the cavity. At variance with the usual treatments, where the mean-field approximation is used to eliminate the z dependence of the field, our model keeps this dependence, thus allowing for the formation of 3D patterns. We have shown that the simultaneous presence of longitudinal and transverse modes leads to the appearance of spatiotemporal pulses, which is confirmed by numerical simulations and experimental results.

ACKNOWLEDGMENTS

APPENDIX A: NUMERICAL EVALUATION OF THE CAVITY FIELD

We have seen that the cavity field E_c can be evaluated as the stationary solution of the cavity and the two-wave mixing device, because of the slow dynamics of the liquid crystals. Thus, E_c on the surface of the photorefractive crystal is adiabatically slaved by n_k and given by Eq. (37). In this appendix we present a strategy to efficiently reduce the numerical errors due to the truncation of the series in Eq. (37).

The operator $\hat{D}$ has eigenvalues λ_k with modulus equal to $\Gamma^{1/2}$, Γ being the fraction of lost photons in each cavity round trip. The series is convergent since $\Gamma^{1/2}<1$ and can be approximated by a finite number N of terms.

Let us assume $J_0(2|\bar{n}_1|)\simeq1$ and $J_1(2|\bar{n}_1|)\bar{n}_1/|\bar{n}_1|\simeq\bar{n}_1$. The root-mean-square error is

$$E_{\mathrm{rms}}^R(N) \equiv \sqrt{\frac{\int dr_\perp \left| \sum_k \sum_{s=N}^\infty \lambda_k^s W_k \right|^2}{\int dr_\perp \left| \sum_k \sum_{s=0}^\infty \lambda_k^s W_k \right|^2}} = \Gamma^{N/2}, \quad \text{(A1)}$$

where W_k are non-normalized cavity eigenmodes, such that $\Sigma_k W_k=\hat{G}E_p$. For large cavity losses, a small number of terms are necessary since many round trips of photons are improbable. Conversely, for high qualities of the cavity, many terms of the series must be evaluated. For $\Gamma=0.8$ and 40 iterations the relative error on E_c is about 1%. This error can be further reduced if an estimate of E_c is known, as occurs in our model. Equation (37) must be solved at every time step and $E_c(t)$ differs slightly from $E_c(t-dt)$, thus the previous value can be used as an estimate of $E_c(t)$. The difference between the exact E_c and the sum of the first N terms is

$$\sum_{s=N}^\infty \hat{D}^s\hat{G}E_p = \hat{D}^N\sum_{s=0}^\infty \hat{D}^s\hat{G}E_p = \hat{D}^N E_c \sim \Gamma^{N/2}E_c. \quad \text{(A2)}$$

Thus,

$$E_c = \sum_{s=0}^{N-1} \hat{D}^s\hat{G}E_p + \hat{D}^N E_c, \quad \text{(A3)}$$

where the second term on the right-hand side is a small correction of the order of $\Gamma^{N/2}E_c$. Let $\tilde{E}_c=E_c+O(dt)$ be the value estimated at the previous time step, then we have that

$$E_c = \sum_{s=0}^{N-1} \hat{D}^s\hat{G}E_p + \hat{D}^N\tilde{E}_c + \Gamma^{N/2}O(dt). \quad \text{(A4)}$$

The second term reduces the relative error by a factor of the order of dt. Furthermore, its evaluation increases only slightly the computation time, as shown by the following algorithm, used to solve Eq. (A4):

$$K_0 = \hat{G}E_p + \hat{D}\tilde{E}_c,$$

$$K_1 = \hat{D}K_0 + \hat{G}E_p,$$

$$K_2 = \hat{D}K_1 + \hat{G}E_p, \quad \dots,$$

$$E_c \simeq K_{N-1} = \hat{D}K_{N-2} + \hat{G}E_p. \quad \text{(A5)}$$

Thus, the error reduction strategy with Eq. (A4) requires to evaluate merely the additional term $\hat{D}\tilde{E}_c$ in the equation for K_0. More precise algorithms are obtained by second-order estimates of $\tilde{E}_c$. In our simulations, we achieved typical precisions of 10^{-6} with merely five terms of the series. The operators $\hat{D}$ and $\hat{G}$ can be easily evaluated by means of fast Fourier transforms, which diagonalize the differential operators in the exponents.

APPENDIX B: CAVITY EIGENMODES

In this appendix we evaluate the cavity eigenmodes without the LCLV and with zero losses. They are the solutions of the following eigenvalue equation:

$$\hat{U}\mathcal{E}_k = e^{-i\Phi_k}\mathcal{E}_k, \tag{B1}$$

where Φ_k is the phase shift of the eigenmode k after a round trip and

$$\hat{U} \equiv \hat{S}^{s_m}\hat{A}(L_{cav} - L_1)\hat{B}(f)\hat{A}(L_1). \tag{B2}$$

Equation (B1) is equivalent to

$$\hat{U}_S\bar{\mathcal{E}}_k = e^{-i\Phi_k}\bar{\mathcal{E}}_k, \tag{B3}$$

where

$$\hat{U}_S \equiv \hat{S}^{s_m}\hat{A}(L_{cav}/2)\hat{B}(f)\hat{A}(L_{cav}/2),$$

$$\bar{\mathcal{E}}_k = e^{[i(L_1 - L_{cav}/2)/2k]\nabla_\perp^2}\mathcal{E}_k. \tag{B4}$$

In order to find the eigenmodes, it is convenient to reduce the operator $\hat{U}_S$ to the exponential of a Hermitian operator. For suitable values of the coefficients C_d and C_l, we have, apart from a unimportant phase factor,

$$\hat{U}_S = e^{-it_c[(-C_d/2)\nabla_\perp^2 + (C_l/2)r_\perp^2]}, \tag{B5}$$

where $t_c \equiv L_{cav}/c$ is the propagation time in one round trip. The cavity with lens is equivalent to a harmonic oscillator with frequency $\omega_\perp = \sqrt{C_d C_l}$. We must evaluate C_d and C_l. In the ray limit, the operators $\hat{A}(L_{cav}/2)$, $\hat{B}(f)$ and $\hat{S}$ correspond, respectively, to the following *ABCD* matrices of the ray transfer matrix analysis (see Sec. III B),

$$\mathcal{A}(L_{cav}/2) = \begin{pmatrix} 1 & L_{cav}/2k \\ 0 & 1 \end{pmatrix}, \quad \mathcal{B}(f) = \begin{pmatrix} 1 & 0 \\ -k/f & 1 \end{pmatrix}$$

$$\mathcal{S} = \begin{pmatrix} -1 & 0 \\ 0 & -1 \end{pmatrix}. \tag{B6}$$

Thus, the overall unitary operator $\hat{U}_S$ is associated to the following *ABCD* matrix,

$$\mathcal{U}_S = (-1)^{s_m} \begin{bmatrix} 1 - \dfrac{L_{cav}}{2f} & \dfrac{L_{cav}}{2k}\left(2 - \dfrac{L_{cav}}{2f}\right) \\ -\dfrac{k}{f} & 1 - \dfrac{L_{cav}}{2f} \end{bmatrix}. \tag{B7}$$

On the other hand, the *ABCD* matrix $\mathcal{U}_S$ from Eq. (B5) is

$$\mathcal{U}_S = \begin{bmatrix} \cos\omega_\perp t_c & \sqrt{\dfrac{C_d}{C_l}}\sin\omega_\perp t_c \\ -\sqrt{\dfrac{C_l}{C_d}}\sin\omega_\perp t_c & \cos\omega_\perp t_c \end{bmatrix}. \tag{B8}$$

From these equations we find that

$$\omega_\perp = \text{sgn}(h_c)\left(\bar{\omega}_\perp - \frac{\pi}{t_c}\theta(-g_c)\right), \tag{B9}$$

where

$$h_c \equiv 1 - \frac{L_{cav}}{2f},$$

$$g_c \equiv \left(1 - \frac{L_{cav}}{2f}\right)(-1)^{s_m},$$

$$\bar{\omega}_\perp = \frac{1}{t_c}\text{asin}\left(\sqrt{\frac{L_{cav}}{f}}\sqrt{1 - \frac{L_{cav}}{4f}}\right), \tag{B10}$$

and θ is the Heaviside function. There are two interesting cases: (a) the number of mirrors s_m is even and $f > L_{cav}/2$; (b) the number of mirrors is odd and $L_{cav}/4 < f < L_{cav}/2$. In both cases, Eq. (B9) reduces to

$$\omega_\perp = \frac{\text{sgn}(h_c)}{t_c}\text{asin}\sqrt{\frac{L_{cav}}{f}\left(1 - \frac{L_{cav}}{4f}\right)}. \tag{B11}$$

$\omega_\perp$ goes to zero for both $f \to \infty$ (plane cavity) and $f \to (L_{cav}/4)^+$ (spherical cavity). The eigenvalues of $\hat{U}_S$ are

$$e^{-i\Phi_k} = e^{-i\omega_\perp(p+q)t_c} \tag{B12}$$

and

$$\Phi_k = [\omega_\perp(p+q) + \omega_\parallel l]t_c, \tag{B13}$$

where p, q, and l are integer numbers and $\omega_\parallel \equiv 2\pi c/L_{cav}$. The two terms $\omega_\perp(p+q)$ and $\omega_\parallel l$ are the transverse and longitudinal cavity frequencies. The corresponding eigenmodes are the Gauss-Hermite functions or, equivalently, the Gauss-Laguerre functions.

The product $C_d C_l$ is equal to $\omega_\perp^2$ and has been evaluated by the diagonal elements of Eqs. (B7) and (B8). The ratio C_d/C_l can be obtained by the off-diagonal elements. In the limit of $f \to \infty$, C_d is obviously equal to L_{cav}/k and C_l is zero.

[1] A. E. Siegman, *Lasers* (Oxford University Press, Oxford, 1986).

[2] J. L. Bougrenet de la Tocnaye, P. Pellat-Finet, and J. P. Huignard, J. Opt. Soc. Am. B **3**, 315 (1986).

[3] F. T. Arecchi, G. Giacomelli, P. L. Ramazza, and S. Residori, Phys. Rev. Lett. **65**, 2531 (1990).

[4] U. Bortolozzo, A. Montina, F. T. Arecchi, J. P. Huignard, and S. Residori, Phys. Rev. Lett. **99**, 023901 (2007).

[5] G. D'Alessandro, Phys. Rev. A **46**, 2791 (1992).

[6] F. T. Arecchi, S. Boccaletti, G. P. Puccioni, P. L. Ramazza, and S. Residori, Chaos **4**, 491 (1994).

[7] B. M. Jost and B. E. A. Saleh, Phys. Rev. A **51**, 1539 (1995).

[8] See EPAPS Document No. E-PLRAAN-76-029710 for two numerical and three experimental movies. In the numerical ones the evolution of the field intensity in the *x-z* plane is shown for two different values of the parameters. The experimental ones show the intensity field in the transverse plane for three dynamical regimes. For more information on EPAPS, see http://www.aip.org/pubservs/epaps.html.

[9] U. Bortolozzo, S. Residori, and J. P. Huignard, Opt. Lett. **31**, 2166 (2006).

[10] A. Brignon, I. Bongrand, B. Loiseaux, and J. P. Huignard, Opt. Lett. **22**, 1855 (1997).

[11] U. Bortolozzo, S. Residori, A. Petrosyan, and J. P. Huignard, Opt. Commun. **263**, 317 (2006).

[12] A. Yariv, *Optical Waves in Crystals* (Wiley, New Jersey, 2003).

[13] See, e.g., *Laser Handbook*, edited by T. Arecchi and E. O. Schulz-Dubois (North-Holland, Amsterdam, 1972).

[14] U. Bortolozzo, P. Villoresi, and P. L. Ramazza, Phys. Rev. Lett. **87**, 274102 (2001).